RSC Advances

PAPER

View Article Online
View Journal | View Issue

Cite this: *RSC Adv.*, 2017, **7**, 53306

Controllable growth of Na_2CO_3 fibers for mesoporous activated alumina ball modification towards the high-efficiency adsorption of HCl gas at low temperature

Shuoyang Liang,[a] Zhengyun Fan,[b] Weidong Zhang,[b] Min Guo,[a] Fangqin Cheng[c] and Mei Zhang *[ac]

Received 29th September 2017
Accepted 6th November 2017

DOI: 10.1039/c7ra10790k

rsc.li/rsc-advances

To fundamentally solve the problem of chlorine corrosion in blast furnace gas (BFG) systems, a supported adsorbent is used for HCl removal at low temperature. In this paper, three alkaline substances, $Ca(OH)_2$, NaOH, and Na_2CO_3, were separately coated on the surface of activated alumina balls (AABs) by wetness impregnation method, using the as-active components. These materials were measured by XRF, XRD, SEM, TEM, and N_2 adsorption to characterize textural properties. The modification experiments indicated that Na_2CO_3 fibers can be obtained on the surface of AABs by adjusting the loading amounts, impregnation time, and drying conditions. The fibers' structure contributes to the gas phase diffusion in the product layer, greatly improving the conversion of Na_2CO_3 (>0.98). The highest value of HCl adsorption capacity reaches 3.56 mmol g^{-1} when the Na_2CO_3 loading amount is 20 wt%, five times the adsorption capacity of pure AABs. The kinetics of HCl removal by the Na_2CO_3 fiber-modified AABs is controlled by the interfacial chemical reaction.

1. Introduction

It has been widely accepted that blast furnace gas (BFG) is a reusable derivative energy source due to the large heat and high pressure in the process of blast furnace production.[1] In the process of recycling the blast furnace gas, the dry-dedusting process is adopted to make the gas purification efficient. However, serious corrosion has appeared in the BFG pipeline in the short term—a large amount of salt blocks the Blast Furnace Top Gas Recovery Turbine Unit (TRT), and even the refractory bricks in the hot blast stove have been partially broken.[2] According to the reports, hydrogen chloride (HCl) in the gas stream is the only explanation for equipment corrosion.[2,3] Normally, the temperature of BFG is in the range of 380–423 K. BFG steam consists of 23% CO, 20% CO_2, 55% N_2, and a small amount of methane; simultaneously, there is about 300 ppm hydrogen chloride (HCl). Although the content of HCl in the BFG is very small, the blast furnace still generates a heavy chlorine burden attributed to the large amount of blast furnace gas production. For example, a 2650 m^3 BF produces 8 million m^3 of BFG per day, containing about 3 tons of HCl, which is a huge threat to the gas pipeline and hot blast stove. Therefore, finding an effective adsorption material to remove HCl from the BFG is urgently necessary.

At present, more studies have paid attention to the removal of acid gases from the hot flue gas (673–1073 K) of the coal industry.[4–11] The reaction mechanism mainly depends on the neutralization of acid and alkali to capture acid gas in the process of gas stream cleaning. Duo *et al.*[5,12] reported that the higher HCl capacity of sorbents correspond to the higher temperature from 573 to 873 K. Na sorbents showed optimal HCl sorption performance in the temperature range of 673–773 K. Dou *et al.*[13,14] found that Na_2CO_3, $Ca(OH)_2$, or CaO were suitable to achieving the tolerance limit of 1 ppmv HCl from hot gas. The experimental results showed that the HCl capacity of alkali materials at 473 K is less than 20% (3.5 mmol HCl g^{-1}) of that at 773 K, suggesting that the chemical reaction of adsorbents is limited at low temperature.[15] Besides, with poor structure, the conversion of the active materials is less than 50%,[16] which undoubtedly increases the cost of dechlorination.

Mesoporous materials such as activated carbon (AC), activated alumina balls (AABs), molecular sieves, *etc.* have been developed as potential adsorbents or catalyst supports for the removal of acidic gases due to their large surface area and abundant porous structure.[17–21] Taguchi *et al.*[22–24] pointed out that the reaction mechanism of gas on the surface of these porous materials relies on physical adsorption, which contributes to regeneration and recycling. ZnO supported by 3-D structural mesoporous molecular

[a]*School of Metallurgical and Ecological Engineering, University of Science and Technology Beijing, Beijing 100083, China. E-mail: zhangmei@ustb.edu.cn; Fax: +86 10 62334926*

[b]*Institute of Technology of Shougang Group, Beijing 100043, China*

[c]*Shanxi Collaborative Innovation Center of High Value-added Utilization of Coal-related Wastes in Shanxi University, China*

sieves had been synthesized for H_2S removal from gas stream, reported by Li,[25] suggesting that the mesoporous structure benefited the dispersion of active phase. Among them, activated alumina balls (AABs) are well known as a potential carrier material for the adsorption of acid gases at low temperature due to their receptivity to modification with alkaline substances.[26–29]

For gases at room temperature, alkaline substances are usually used as active materials, supported by impregnation method, to remove acid gas for feeding molten carbonate fuel cells (MCFCs).[30–33] Lee[34] showed that the HCl capacity of NaOH/AC is about 6 times that of commercial alumina. However, Micoli *et al.*[35,36] investigated the HCl adsorption performance of activated carbon impregnated with KOH, NaOH or Na_2CO_3, respectively. They suggested that the best adsorption performance for HCl adsorption was obtained by impregnating Na_2CO_3. Due to temperature limits, the chlorine capacity of the sorbent was lower than 0.4 mmol HCl g^{-1}. Zhao *et al.*[37–39] suggested that K_2CO_3/Al_2O_3 and Na_2CO_3/Al_2O_3 had the potential to be employed as excellent sorbents for CO_2 uptake due to their rapid reaction rate and high CO_2 capture capacities. Zhao[40] investigated the effect of Na_2CO_3 loading on the adsorption capacity of the acid gases, which reached a maximum at the dispersion threshold. The paper of Dong[41] showed that there was a change of surface structure after the modification of γ-Al_2O_3 with Na_2CO_3, unfortunately without any further analysis. It is worth mentioning that the change of HCl concentration in mixed gas has little effect on the adsorption capacity in the adsorption test.[5,34] Therefore, many experiments to simulate the removal of HCl from gas tend to adopt an accelerated aging test with high HCl concentration.

In general, there is a lack of literature on HCl removal from BFG in the steel industry for its extreme conditions, namely, selective removal of HCl at the lower temperature of 380–423 K. For the purpose of environmental protection and energy recovery, the importance of HCl removal from blast furnace gas is self-evident. In this work, three modifiers, Na_2CO_3, $Ca(OH)_2$ and NaOH, were coated on AABs by impregnation method. The structure properties of the initial, impregnated and exhausted materials have been characterized. The adsorption activity of the prepared materials had been measured using the accelerated aging test with a HCl concentration of 50% at the low temperature of 423 K; accordingly, the reaction mechanism of HCl and sorbents are also proposed.

2. Experimental

2.1 Materials

Commercial activated alumina balls (AABs) were purchased from Shandong province in China without further purification. Calcium hydroxide ($Ca(OH)_2$), sodium carbonate anhydrous (Na_2CO_3), and sodium hydroxide (NaOH) were analytical grade and used as received without further purification. The basic physical properties of AABs are shown in Table 1.

2.2 Preparation of modified sorbents

The modified sorbents in this study were prepared by the impregnation method. The preparation process consisted of two stages, namely, the selection of modifiers and optimization of impregnating conditions.

Table 1 The physical properties of AABs

Properties	Particle size (mm)	S_{BET} (m^2 g^{-1})	Pore volume (cm^3 g^{-1})	Pore size (nm)
Parameter	4–8	160	0.45	9.74

2.2.1 Alkaline modifier selection. The impregnation solutions were obtained by dissolving 0.34 g $Ca(OH)_2$ powder, 20 g NaOH powder and 20 g Na_2CO_3 powder in 200 mL of deionized water, respectively, to form three kinds of impregnation solutions. Then, 40 g AABs were severally added into the impregnation solutions, which were then subjected to ultrasonic shocking at room temperature for 1 h, immersion for 17 h and finally drying at 473 K for 24 h. The obtained samples were named $Ca(OH)_2$-AAB, 10NaOH-AAB, and 10Na_2CO_3-AAB, respectively; 10 represents the designed loading amounts of NaOH and Na_2CO_3, whereas the loading amount of $Ca(OH)_2$ is the maximum value for its lower solubility. The pure AABs without alkaline modification were used for comparison. The actual loading amounts of NaOH and Na_2CO_3 on the sorbents were determined by X-ray fluorescence (XRF).

2.2.2 Impregnation parameters selection. In order to optimize the microstructure of sorbents, factors such as loading amounts of Na_2CO_3, impregnation time and drying time have been investigated; the details of influencing factors are shown in Table 2. To prepare the impregnation solution, 10 g, 30 g, 40 g, 50 g and 60 g pure Na_2CO_3 powder were separately placed in 200 mL of deionized water resulting in, respectively, 0.47 mol L^{-1}, 1.42 mol L^{-1}, 1.88 mol L^{-1}, 2.36 mol L^{-1} and 2.83 mol L^{-1} Na_2CO_3 solutions, and five sorbents of different Na_2CO_3 loading amounts were obtained after 40 g AABs had been impregnated in the corresponding Na_2CO_3 solution. The designations of 5, 15, 20, 25 and 30 correspond to the percentage of Na_2CO_3 loading amounts. The effects of the impregnation time (2 h, 10 h, 17 h and 24 h) and drying time (16 h, 20 h, 24 h and 28 h) on the microstructure of sorbents were subsequently investigated. The actual loading amounts of Na_2CO_3 on the sorbents were determined by XRF.

2.3 Activity test of HCl removal

After the preparation of modified sorbent loaded with Na_2CO_3, its HCl removal activity was subsequently tested in a fixed bed reactor with the reaction temperature of 423 K under normal atmosphere. The experimental apparatus is shown in Fig. 1. The sorbents were firstly treated at 423 K for 0.5 h in N_2 flow

Table 2 Summary of impregnation conditions

Modifier	Factors	Parameters
Na_2CO_3	Loading amounts	5%, 15%, 20% 25%
	Impregnation time	2 h, 10 h, 17 h, 24 h
	Drying time	16 h, 20 h, 24 h, 28 h

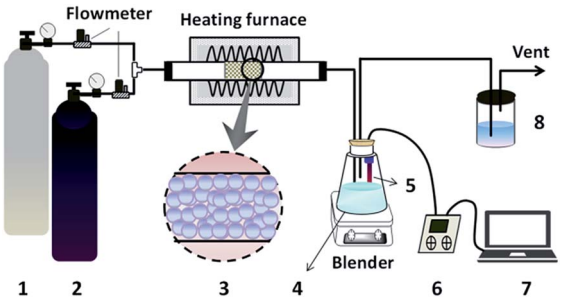

Fig. 1 Schematic diagram of the experimental apparatus: 1-N_2 cylinder, 2-HCl cylinder, 3-sorbents, 4-adsorption bottle, 5-pH electrode, 6-pH meter, 7-computer, 8-treatment bottle.

(20 mL min^{-1}) before the test. High-purity HCl and N_2, whose flow rates were similarly controlled by mass flow meters at 20 mL min^{-1}, were mixed to pass through the sorbents (about 23 g) in the heating furnace. Because the work temperature of BFG is in the range of 380–423 K, the experimental temperature for HCl adsorption was controlled at 423 K to simulate the real temperature of BFG. Afterwards, the escaped HCl was absorbed by 1 L deionized water in the adsorption bottle, and the concentration C_t of HCl in the outlet gas at that moment was ascertained synchronously by detecting the change of the pH value in the adsorption solution.[35,36,42] Finally, the gas stream flowed through the treatment bottle, ensuring no pollution to the environment before the vent.

The test was stopped immediately when the pH value decreased sharply in the adsorption bottle; this moment was named the breakthrough time t_b. The exhausted sorbents were taken out of the reactor and desorbed in the deionized water, and the concentration C_e of chloride ion in the desorption solution was determined by a chloride ion concentration meter.

The HCl adsorption capacity q_e (mmol g^{-1}) of the exhausted sorbents can be calculated from the following eqn (1):

$$q_e = \frac{VC_e}{m_0} \times 1000 \quad (1)$$

where m_0 (g) is the initial mass of sorbents, V (L) is the volume of the desorption solution, and C_e (mol L^{-1}) is the concentration of Cl^- in the desorption solution at equilibrium.

The adsorption efficiency η of the sorbents at every moment can be calculated using the following eqn (2):

$$\eta = \frac{1 - C_t}{C_0} \times 100\% \quad (2)$$

where C_0 (constant, 20 mL min^{-1}) represents the concentration of HCl in the inlet gas, and C_t (mL min^{-1}) represents the concentration of HCl in the outlet gas at time t.

2.4 Characterizations

The actual loading amounts of Na_2CO_3 supported on the sorbents were determined by X-ray fluorescence spectrometer (XRF-1800, Japan). The field emission scanning electron microscope (FESEM) (Zeiss supra 55), operated at 10 kV, coupled with energy dispersive X-ray analysis (EDS) was used to investigate the morphologies and element distribution of sorbent nanostructures. The X-ray diffraction (XRD) analysis, carried out on a powder X-ray diffractometer (Rigaku Dmax-2500 diffractometer using Cu Kα radiation), was used to determine the phase composition of the sorbents. Further structural characterization of the Na_2CO_3 fibers coated on the AABs substrate was performed by applying high-resolution transmission electron microscopy (HRTEM, Tecnai F20) operated at 200 kV. Surface area measurements were carried out by N_2 adsorption at 77 K using a Micromeritics ASAP2020 instrument. The pH value of the adsorption solution was monitored by pH electrode 201T-M connected to the pH meter (MP520, Shanghai, San-Xin). The chloride ion concentration in the HCl desorption solution was measured by chloride ion – selective electrode CL502 connected concentration meter (MP523, Shanghai, San-Xin).

3. Results and discussion

3.1 Preparation of the alkaline modified sorbents

3.1.1 Selection of modifier. Three alkali-modified sorbents, namely, $Ca(OH)_2$-AAB, 10NaOH-AAB and 10Na_2CO_3-AAB, were characterized by SEM, XRD and BET. The loading amounts and BET results are summarized in Table 3. It can be observed that the loading amount of Na_2CO_3 is the same as NaOH. However, the amount of $Ca(OH)_2$ impregnated was less than 1 wt%. The BET results showed that the specific surface area and pore volume of 10NaOH-AAB were greatly reduced. In contrast, the sample 10Na_2CO_3-AAB retained the specific surface area after loading with Na_2CO_3 solution.

The XRD patterns of the modified samples are shown in Fig. 2. It depicts that sample $Ca(OH)_2$-AAB shows corresponding characteristic peaks of the substrate, whereas sample 10NaOH-AAB shows trace peaks of $NaAlO_2$ compared with the obvious peaks of Na_2CO_3 phase in sample 10Na_2CO_3-AAB besides the substrate, suggesting that a complex reaction between NaOH and the AAB substrate has occurred.

The SEM images of the untreated and modified AABs with alkaline substances are shown in Fig. 2(b–e). From Fig. 2(b), it can be seen that there were a large number of fluffy structures on the surface of the original AABs, which makes its specific surface area large and benefits the alkaline adsorption. The modification of $Ca(OH)_2$ as presented in Fig. 2(c) generates some lamellar structures in the AABs. However, the modification of NaOH deteriorates the surface morphology of alumina balls; namely, the pores in the AABs are almost blocked (Fig. 2(d)). The microscopic morphology of sorbent 10Na_2CO_3-AAB is shown in Fig. 2(e); a layer of fibrous network coats the surface of AABs, indicating that the Na_2CO_3 fibers on the support help to preserve its high surface area. Considering the surface morphology and physical properties of the sorbent after modification, Na_2CO_3 has been selected as the optimal modifier.

3.1.2 Effect of Na_2CO_3 loading amount. The relationship curve of the actual loading amounts of Na_2CO_3 on the sorbents with the designed loading amounts is shown in Fig. 3(a). The actual loading amount of Na_2CO_3 increased synchronously with

Table 3 The loading amounts and BET results of the AABs with or without modification

Samples	AAB	$Ca(OH)_2$-AAB	10NaOH-AAB	10Na_2CO_3-AAB
Designed loading amount (wt%)	—	0.34	10	10
Loading amount (wt%)	—	5	98	98
S_{BET} (m^2 g^{-1})	160	125	105	144
Pore volume (cm^3 g^{-1})	0.45	0.51	0.40	0.51
Pore diameter (nm)	9.74	6.59	9.32	7.9

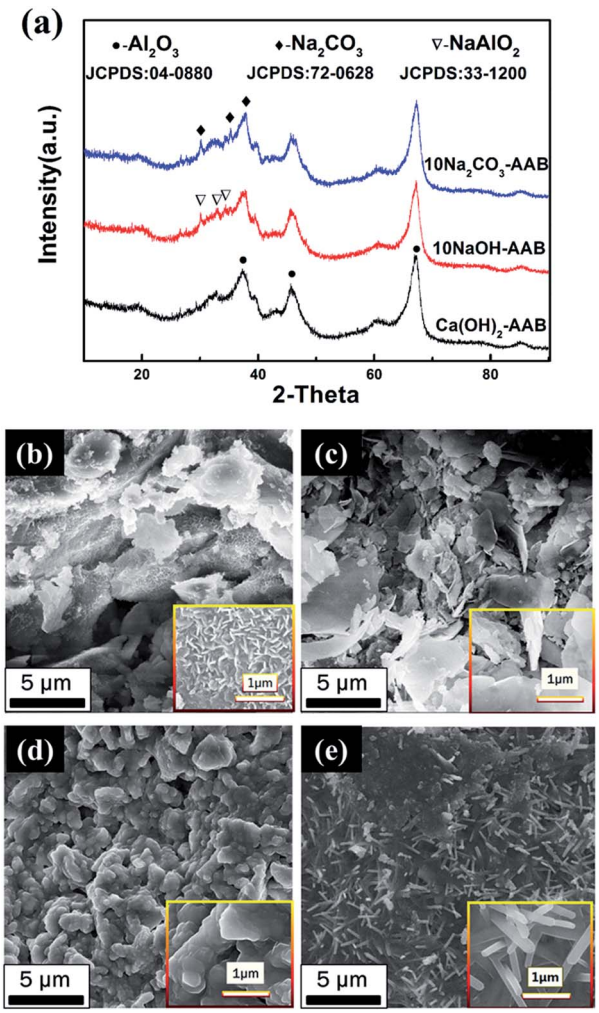

Fig. 2 (a) XRD patterns of the modified sorbents with different alkaline substances. The SEM images of the untreated and modified sorbents: (b) AABs, (c) $Ca(OH)_2$-AAB, (d) 10NaOH-AAB and (e) 10Na_2CO_3-AAB.

the increasing concentration of Na_2CO_3 solution up to 20 wt%, and then it continued to increase, but slowly.

Moreover, the actual loading capacities are almost accorded to the concentration of Na_2CO_3 solution when it is lower than 25 wt%, indicating that the loading amount of Na_2CO_3 in the sorbents reached saturation herein. Therefore, the loading amounts ranging from 5 wt% to 25 wt% is suitable for further investigation.

The XRD patterns of different loading amounts are shown in Fig. 3(b). When the loading amount reaches 10 wt%, the slight characteristic peaks of Na_2CO_3 can be detected in the XRD patterns. When the loading amount increases to 15 wt% and even higher, the characteristic peaks of Na_2CO_3 are obvious. There is no new phase formation in the entire process, indicating that no chemical reaction happened between Na_2CO_3 and AABs. The BET results of the samples with different loading amounts are listed in Table 4. It shows that the specific surface area of the sorbent decreases first and then increases with the increasing loading amounts, and reaches the highest value of 150 m^2 g^{-1} when loading amount is 15 wt%. The specific surface area of the sorbent obviously reduces when the loading amount is further increased to 25 wt%, suggesting that there must be a great change in AAB microstructure.

The FESEM images of modified AABs with different loading amounts of Na_2CO_3 are shown in Fig. 4(a–d). Clearly, the surface morphology of the samples changes greatly with different loading amounts. When the loading amount is 5 wt%, the

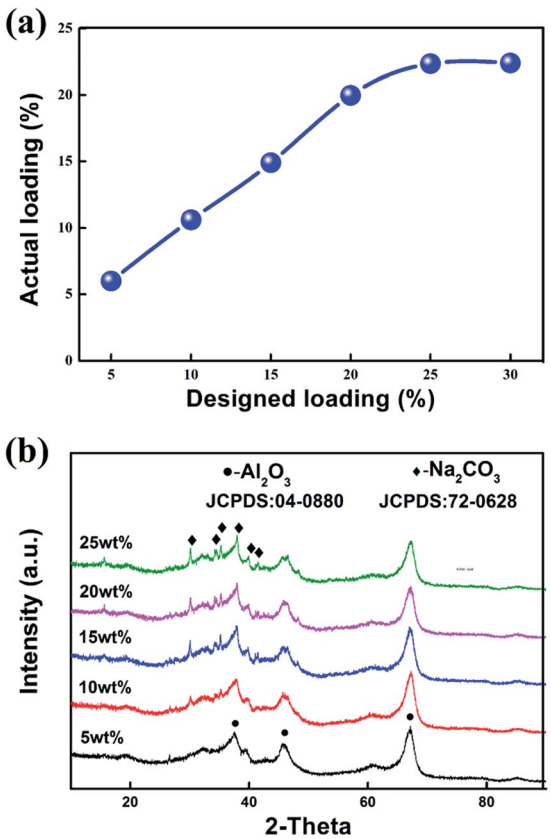

Fig. 3 (a) The curve of actual loading amount against the designed loading amount and (b) XRD patterns of the modified sorbents with different loading amounts: 0–25 wt%.

Table 4 The BET results of the sorbents with different loading amounts

Loading amount (wt%)	Surface area ($m^2\ g^{-1}$)	Pore volume ($cm^3\ g^{-1}$)	Pore diameter (nm)
5	125	0.48	7.6
10	144	0.51	7.9
15	150	0.45	5.65
20	145	0.45	7.8
25	134	0.42	6.6

surface of the sample shows a small number of fibers growing along the edge of AAB pores, meanwhile blocking most of the fluffy structures. Further enhancing the loading amount to 15–20 wt%, the fibers on the surface of the samples reach their longest; that is, the fibers have an average length longer than 20 μm, the average aspect ratio is more than 100, and they uniformly cover the surface of AABs, which greatly improves the active sites of sorbents. When the loading amount increased to 25 wt%, almost all the fibers disappeared, and the surface of AABs are covered completely by a thick layer of Na_2CO_3. The SEM results can explain the BET variation.

In order to analyze and understand the cause of formation and the phase composition of fibers, XRD, SEM and TEM of modified AABs with 15 wt% loading were subsequently detected. The EDS result in Fig. 4(e) shows that fibers consist of elements Na and Al, suggesting that Na_2CO_3 may be adsorbed on the Al_2O_3 substrate. Furthermore, detection of Al illustrates that the surface of the Al_2O_3 substrate has not been completely enclosed, which benefits the effective utilization of the porous structure of the Al_2O_3 substrate. Fig. 4(g) shows a typical TEM image of the fibers. The crystal plane distance measured by the lattice fringe is 0.237 nm or 0.238 nm in Fig. 4(h), which is similar to the (112) lattice spacing of Na_2CO_3 (0.237 nm, PDF card no. 72-0628). Furthermore, it can be found that the Na_2CO_3 fiber shows a stronger diffraction peak of (112) in Fig. 4(f), suggesting that the growth of fibers is oriented along the [112] direction.

The pore volume distribution of the six samples is shown in Fig. 5. It can be seen that the pore volume distribution of modified samples concentrates in the range of 5–10 nm and that the samples exhibit almost uniform mesoporous structure, which agrees well with the result of SEM observation.

3.1.3 Effect of impregnation time. The FESEM images of AABs modified at different durations (2 h, 10 h, 17 h and 24 h) in the impregnation solution and then dried at 473 K for 24 h are separately shown in Fig. 6. It shows that the surface morphology of the samples transformed obviously with prolonged impregnation time. When the impregnation time is less than 10 h, no Na_2CO_3 fiber appears on the surface of the sample. The Na_2CO_3 fibers achieve maximum and uniform coverage on the surface of AABs when the impregnation time reaches 17 h. When the

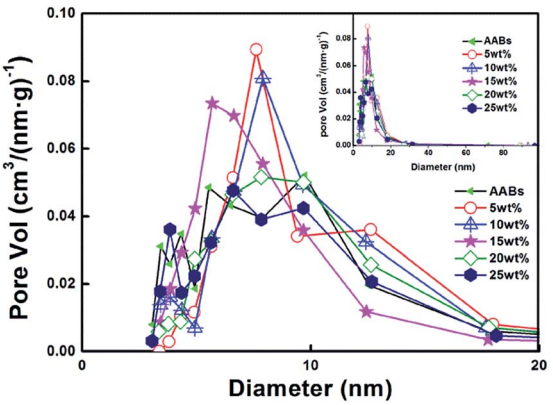

Fig. 5 Pore volume distribution of the modified sorbents with different loading amounts: 0–25 wt%, inset image is the full view of the pore volume distribution.

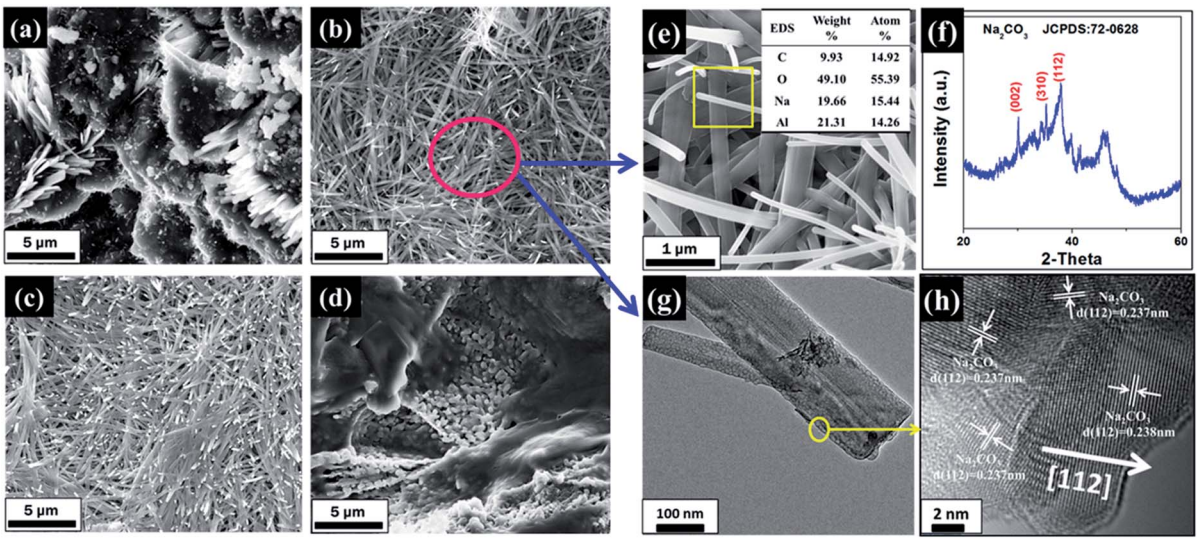

Fig. 4 Representative FESEM images of modified AABs with different loading amounts of Na_2CO_3: (a) 5 wt%, (b) 15 wt%, (c) 20 wt%, (d) 25 wt%, and (e) typical SEM-EDS analysis of the fibers, (f) XRD pattern of the modified AABs (15 wt%), and (g) TEM and (h) HRTEM images of the fiber.

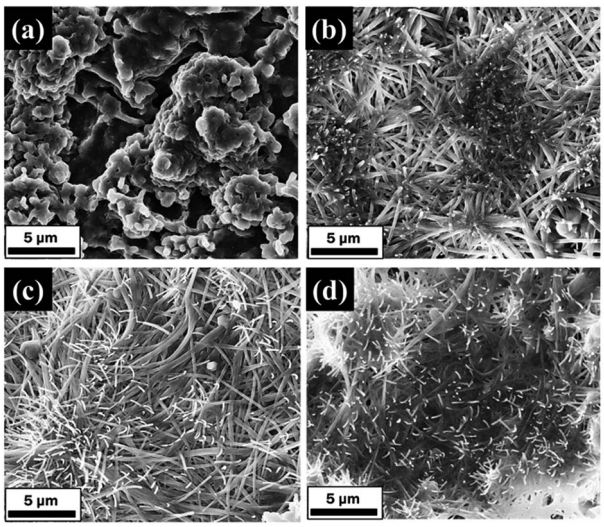

Fig. 6 FESEM images of modified AABs (20 wt%) with different impregnation time: (a) 2 h, (b) 10 h, (c) 17 h, (d) 24 h (impregnation conditions: drying for 24 h at 473 K).

impregnation time is more than 24 h, however, the Na_2CO_3 fibers on the substrate surface bond together, suggesting that impregnation for too long a time inhibited the growth of Na_2CO_3 fibers. Hence, the Na_2CO_3 fibers on the surface of the modified AABs only appear with maximum and uniform coverage after 17 h impregnation.

3.1.4 Effect of drying time. After immersion in 20 wt% Na_2CO_3 solution for 17 h, the sorbents were dried from 16 h to 28 h in an oven (423 K). Their microstructures are shown in Fig. 7. Similarly, Na_2CO_3 fibers show obvious differences under different drying time. When the drying time is 16 h, the bud of the Na_2CO_3 fibers just grew on the surface of the AABs. With prolonged drying time to 24 h, the Na_2CO_3 fibers are also observed on the surface of AABs. However, when the drying time is further extended, the Na_2CO_3 fibers stopped further growth, suggesting that the production of fibers achieved equilibrium due to the complete exhaustion of moisture.

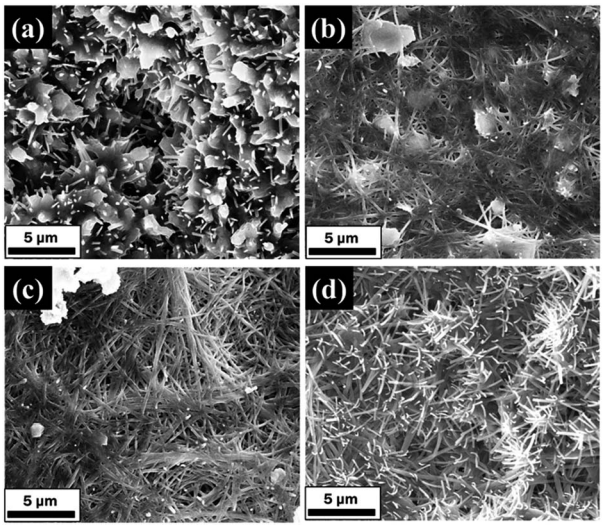

Fig. 7 FESEM images of modified AABs (20 wt%) at different drying time: (a) 16 h, (b) 20 h, (c) 24 h, (d) 28 h (impregnation conditions: impregnation time is 17 h, drying at 473 K).

The wetness impregnation method was used to support Na_2CO_3 on AABs to obtain the modified sorbents. Na_2CO_3 fibers are controlled to grow on the AAB surface by adjusting the loading amount, the impregnation time and the drying time. The optimal conditions for fiber growth are a loading amount of 15–20 wt%, impregnation time of 17 h and drying at 473 K for 24 h.

3.2 HCl adsorption measurement

After the AABs were modified with the Na_2CO_3 fibers, the HCl removal experiments were carried out. In this study, the principle of HCl removal is an acid–base reaction, as shown in eqn (3).

$$Na_2CO_3 + 2HCl = 2NaCl + CO_2 + H_2O \quad (3)$$

The capture of HCl involved firstly the physical selective adsorption on the surface of Na_2CO_3 fibers, followed by the acid–base reaction, forming NaCl crystals on the sorbent surface along with CO_2, which escapes out.

The total conversion rate X_e of Na_2CO_3 can be adopted to evaluate the reaction degree, which is depicted as eqn (4):

$$X_e = \frac{M_N(q_e - q_0)}{2 \times \frac{A}{1+A} \times 1000} \quad (4)$$

where M_N is the molecular weight of Na_2CO_3 (106 g mol^{-1}), A (wt%) is the initial loading amount of Na_2CO_3, q_0 (mmol g^{-1}) is the HCl adsorption capacity of the AABs, and q_e (mmol g^{-1}) is the HCl adsorption capacity of the modified AABs.

3.2.1 Reaction product analysis. The surface morphology image of the exhausted sorbent with 20 wt% loading is obviously different from the original sorbents, as shown in Fig. 8(a). The elemental distribution of the energy spectrum, shown in Fig. 8(b), suggests that the phases on the surface of the sorbent are almost entirely NaCl and Al_2O_3 (carbon had been sprayed for electrical conduction). The XRD patterns of exhausted sorbents are shown in Fig. 8(c); they contain the characteristic peak of NaCl besides the substrate, indicating again that the solid-phase product of the reaction is only NaCl.

3.2.2 Adsorption efficiency analysis. The pH evolution curves and the adsorption efficiency η curves of the sorbents with different loading amounts are shown in Fig. 9. It can be seen that the pH value is almost kept constant during the whole adsorption process for the AAB sorbents before breakthrough (Fig. 9(a)), indicating that the physical adsorption of HCl is efficient, with the breakthrough time of 37 min. However, the breakthrough time is significantly delayed with the increase of the Na_2CO_3 loading amounts (Fig. 9(b)), suggesting that the adsorption performance has been improved by chemical adsorption, and the longest breakthrough time of 120 min is obtained with the loading amount of 20 wt% and 25 wt%. As shown in Fig. 9(c) of the enlarged curves, there is a clear

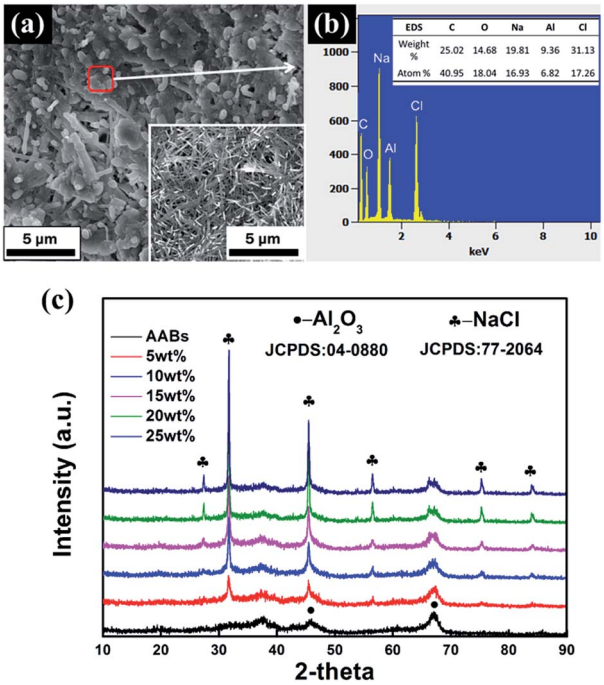

Fig. 8 (a) FESEM image and (b) typical EDS spectrum of the exhausted sorbent with 20 wt% loading; (c) XRD patterns of the exhausted sorbents with different loading amounts: 0–25 wt%. The inset image in (a) presents the original microstructure of the fibers.

reduction of pH value in the modified adsorbents, at which the physical adsorption is suppressed; meanwhile, the chemical reaction increases slowly, and it is named as transition time t_c. The breakthrough times t_b and transition times t_c are shown in Fig. 9(d).

The physical adsorption processes of these modified sorbents are far less than the AABs, suggesting that Na_2CO_3 has blocked the original pores of AABs. When the neutralization reaction between HCl and Na_2CO_3 is faster than the physical adsorption, the overall adsorption efficiency is only attributed to the chemical adsorption, where the sorbents completely capture the HCl. After the sorbent was consumed to a certain extent, HCl adsorption stopped, and the adsorption efficiency dropped dramatically (Fig. 9(b)); the sorbents became ineffective.

3.2.3 Adsorption capacity analysis. The HCl adsorptive capacity q_e and final conversion ratio of Na_2CO_3 X_e were calculated by eqn (1) and (4). The curves of q_e and X_e with different loading amounts of Na_2CO_3 are shown in Fig. 10. It can be observed that the highest value of q_e reaches 3.56 mmol g^{-1}, which is five times the adsorption capacity of AABs. Meanwhile, it keeps a conversion ratio higher than 0.98 before the sorbents have been exhausted. When the loading amount increased to 25 wt%, the conversion ratio of Na_2CO_3 decreased from 0.98 to 0.90. The conversion of the Na_2CO_3 obtained in this study is higher than that of the previously reported ones in literature, summarized in Table 5.

3.2.4 Kinetics of HCl adsorption. In order to elucidate the reaction mechanism of HCl adsorption by AAB modified with

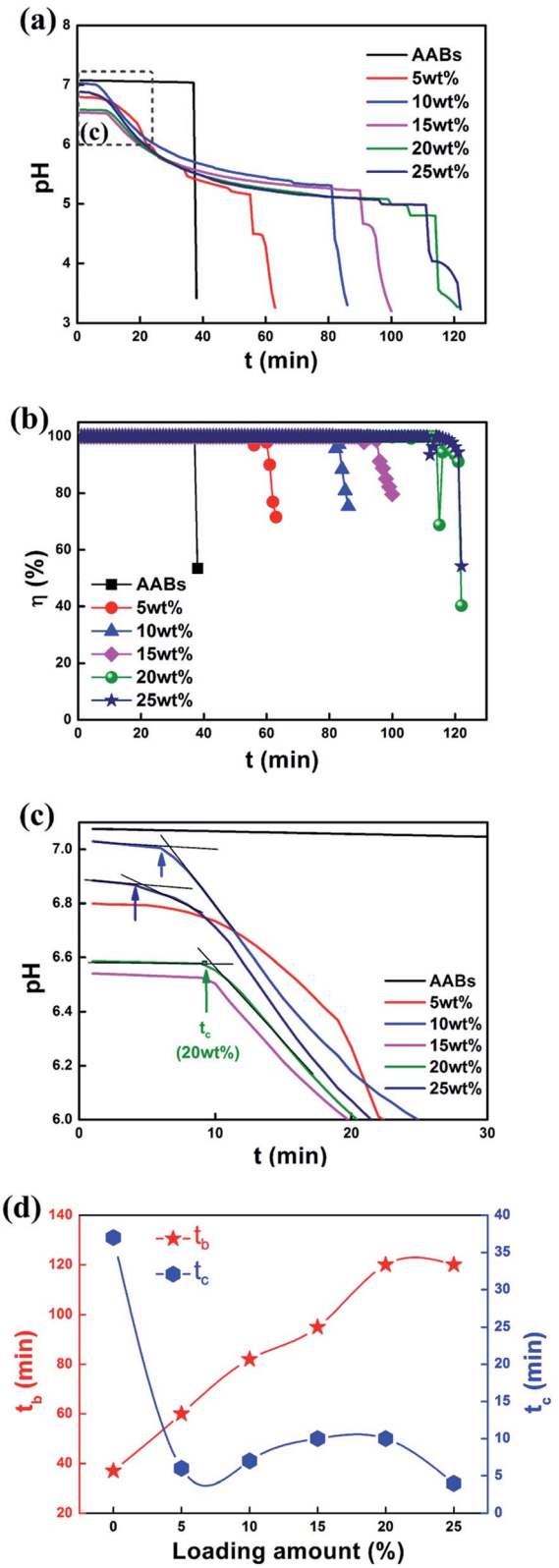

Fig. 9 (a) The pH evolution curves and (b) the adsorption efficiency η curves of the sorbents with different loading amounts: 0–25 wt%. (c) The enlarged curves of (a) in the early 30 min period; (d) the curves of breakthrough time t_b and transition time t_c.

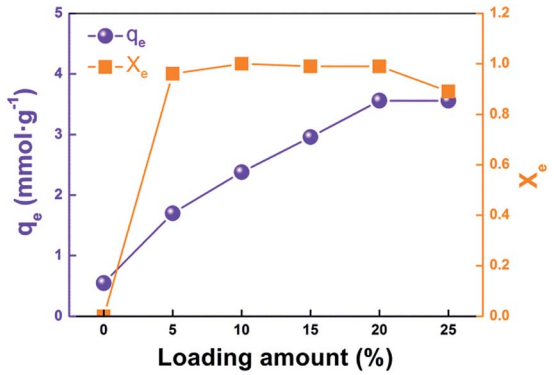

Fig. 10 The curves of adsorption capacity q_e and conversion ratio of Na_2CO_3 X_e *vs.* loading amounts.

Na_2CO_3 fibers, some models have been fitted to explain the kinetics of HCl adsorption at 423 K. The process of HCl adsorption can be divided into the following four steps:

(1) The HCl gas adsorbs on the surface of the Na_2CO_3 fibers.

(2) HCl and Na_2CO_3 molecules react on the surface of Na_2CO_3 fibers, generating H_2O, NaCl and CO_2.

(3) The CO_2 molecules escape outwardly into the gas stream through the product layer; H_2O molecules, combined with fresh HCl molecules, diffuse to the inside surface of unreacted fibers.

(4) When the reaction rate of HCl and Na_2CO_3 quickly reduces, the sorbents become exhausted.

In this study, the principle of HCl adsorption is shown in eqn (3). The conversion ratio with per-minute X_t can be calculated to investigate the kinetics of HCl adsorption, as shown in eqn (5):

$$X_t = X_e \times \frac{\int_{t_c}^{t} \eta dt}{\int_{t_c}^{t_b} \eta dt} \quad (t > t_c) \tag{5}$$

where X_e represents the maximum conversion rate, shown in Fig. 10, η (%) represents the adsorption efficiency of the sorbent at the time t, t_b (min) is the breakthrough time of the sorbents, and t_c (min) is the transition time of the sorbents.

Considering the pore size distribution of the sorbent, the vast majority of the mesopores do not govern the entry or exit of the gas; that is, the external diffusion of the gas never becomes the rate-limiting link of the adsorption reaction. According to the previous reports,[42–46] the reaction kinetics of sorbents and HCl in the reaction of HCl adsorption at high temperature is mainly controlled by diffusion in the product layer or interfacial chemical reaction.

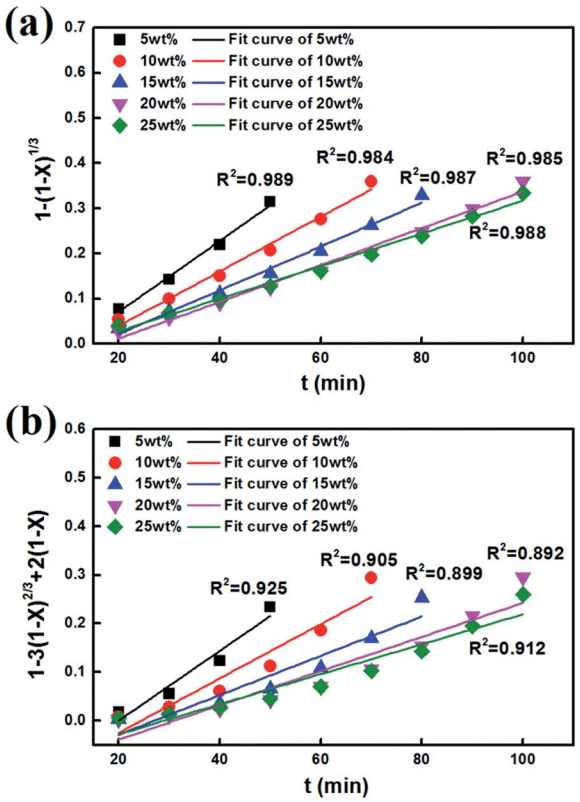

Fig. 11 Correlation of X with time t: (a) interfacial chemical reaction control, (b) product layer diffusion control.

If reaction is controlled by the interfacial chemical reaction at the grain surface, it will follow eqn (6):[9,13,44]

$$g(X) = 1 - (1 - X)^{\frac{1}{3}} = K_1 t \tag{6}$$

where t is the reaction time and K_1 represents the reaction rate constant.

Table 5 Comparison of adsorption temperature and breakthrough performance with reported literatures[a]

Adsorbent	Percentage of active components	Gas flow rate (mL min^{-1})	Adsorption T (K)	Breakthrough HCl capacity/mmol g^{-1}	Conversion rate	Ref.
$Na_2CO_3 \cdot 10H_2O$	—	250	673–773	—	0.49	5
$Ca(OH)_2$	—	150	443	—	~0.15	15
Limestone/Al_2O_3	30 wt%	1400	1123	—	~0.6	16
CN1$^{\#}$	—	3000 (h^{-1})$^{\alpha}$	823	4.1	~0.4	14
NaOH/AC$^{\$}$	8 wt%	100	308	0.05	—	36
Na_2CO_3/AC$^{\$}$	5 wt%	100	308	0.33	—	36
K_2CO_3/Al_2O_3	40 wt%	500	673	6.28	0.75	29
Na_2CO_3/Al_2O_3	**20 wt%**	**40**	**423**	**3.56**	**0.98**	**This study**

[a] CN1$^{\#}$ is $Na_{0.98}Mg_{0.25}Ca_{2.3}O_{3.04}$, mixed with binders and texturing agents. AC$^{\$}$ is activated carbon. (h^{-1})$^{\alpha}$ is the unit of space velocity.

If the reaction is controlled by reactant diffusion through the product layer, it will follow eqn (7):

$$p(X) = 1 - 3(1 - X)^{\frac{2}{3}} + 2(1 - X) = K_2 t \quad (7)$$

where K_2 represents the reaction rate constant.

After fitting the experimental data to eqn (6) and (7), the calculated results are separately shown in Fig. 11(a) and (b). Compared with correlation coefficient, the figure shows that the model of the interfacial chemical reaction control could better explain the experimental results; especially, the linear fitting coefficient R^2 of the modified AABs is larger than 0.980, proving that the adsorption reaction is completely controlled by the interfacial chemical reaction. On one hand, the Na_2CO_3 fibers did not block the fluffy structures on the surface of original AABs as shown in Fig. 2(b) and maintained the large specific surface area of the AABs; on the other hand, the uniform pore distribution of Na_2CO_3 fibers provided many convenient channels for the gas inward and outward, both resulting in the easier diffusion of gas phase in the product layer. In this case, internal diffusion of gas phase will no longer be the rate-limiting step in the process of chemical adsorption.

4. Conclusions

In this paper, alkali-modified AABs have been prepared to evaluate their performance for HCl adsorption at low temperature (423 K). The results have demonstrated better modification ability of Na_2CO_3 compared to $Ca(OH)_2$ or NaOH. A typical fibrous structure was obtained on the surface of the sorbent by loading Na_2CO_3. The loading amounts, impregnation time and drying time had great impact on the morphology of Na_2CO_3 fibers. When the loading amount was 15–20 wt%, the impregnation time was 17 h, and the drying time was 24 h, Na_2CO_3 fibers with good orientation and high aspect ratio could be obtained.

In addition, the HCl adsorption performance was investigated in a fixed bed reactor at 423 K. Extremely high adsorption efficiency and the highest adsorption capacity of 3.56 mmol HCl g^{-1} were achieved when the loading amount was 20 wt%; the adsorption capacity of the modified sorbents is five times that of AABs. The physical adsorption is faster than chemical adsorption in the initial process of HCl adsorption, and then the dominant reaction strongly depends on the chemical adsorption. The kinetics investigation indicates that the reaction is controlled by the interfacial chemical reaction; the diffusion of gas phase in the product layer has been greatly improved by the fiber structure. We believe that Na_2CO_3 fiber-impregnated AABs are promising for the commercial application of HCl removal from BFG.

Conflicts of interest

There are no conflicts to declare.

Acknowledgements

This work was financially supported by the National Natural Science Foundation of China (51672025, 51572020, 51372019), and Major Projects of Science and Technology in Shanxi Province (MC2016-03).

Notes and references

1 K. Goto, H. Okabe, F. A. Chowdhury, S. Shimizu, Y. Fujioka and M. Onoda, *Int. J. Greenhouse Gas Control*, 2011, **5**, 1214–1219.
2 B. S. Hu, Y. L. Gui, G. Y. Hu, K. Lv and C. Y. Song, *Environ. Eng.*, 2016, **34**, 78–80.
3 B. Zhang, B. S. Hu, Y. L. Gui, X. G. Liu and G. Y. Hu, *Mod. Chem. Ind.*, 2016, **36**, 137–140.
4 R. Bie, S. Li and L. Yang, *Chem. Eng. Sci.*, 2005, **60**, 609–616.
5 W. Duo and N. F. Kirkby, *Chem. Eng. Sci.*, 1996, **51**, 2541–2546.
6 A. D. Lawrence and J. Bu, *Chem. Eng. Sci.*, 2000, **55**, 6129–6137.
7 W. Duo, N. F. Kirkby, J. P. K. Seville and R. Clift, *Chem. Eng. Sci.*, 1995, **50**, 2017–2027.
8 H. Matsuda, S. Ozawa, K. Naruse, K. Ito, Y. Kojima and T. Yanase, *Chem. Eng. Sci.*, 2005, **60**, 545–552.
9 B. L. Dou, C. Wang, H. S. Chen, Y. C. Song, B. Z. Xie, Y. J. Xu and C. Q. Tan, *Chem. Eng. Res. Des.*, 2012, **90**, 1901–1917.
10 G. M. Lin and C. S. Chyang, *Energy Fuels*, 2016, **30**, 10696–10704.
11 M. Nunokawa, M. Kobayashi and H. Shirai, *Powder Technol.*, 2008, **180**, 216–221.
12 W. Duo, J. P. K. Sevill, N. F. Kirkby and R. Clift, *Chem. Eng. Sci.*, 1994, **49**, 4429–4442.
13 B. L. Dou, B. B. Chen, J. S. Gao and X. Z. Sha, *Energy Fuels*, 2005, **19**, 2229–2234.
14 B. Dou, W. Pan, J. Ren, B. Chen, J. Hwang and T.-U. Yu, *Energy Fuels*, 2007, **21**, 1019–1023.
15 R. Yan, T. Chin, D. T. Liang, K. Laursen, W. Y. Ong, K. Yao and J. H. Tay, *Environ. Sci. Technol.*, 2003, **37**, 2556–2562.
16 J. Partanen, P. Backman, R. Backman and M. Hupa, *Fuel*, 2005, **84**, 1664–1673.
17 C. Yang, L. L. Gao, Y. X. Wang, X. K. Tian and S. Komarneni, *Microporous Mesoporous Mater.*, 2014, **197**, 156–163.
18 Z. R. Zhang, R. W. Hicks, T. R. Pauly and T. J. Pinnavaia, *J. Am. Chem. Soc.*, 2001, **124**, 1592–1593.
19 T. J. Bandosz, *Carbon*, 1999, **37**, 483–491.
20 M. Balsamo, S. Cimino, G. de Falco, A. Erto and L. Lisi, *Chem. Eng. J.*, 2016, **304**, 399–407.
21 M. C. Castrillon, K. O. Moura, C. A. Alves, M. Bastos-Neto, D. C. S. Azevedo, J. Hofmann, J. Möllmer, W.-D. Einicke and R. Gläser, *Energy Fuels*, 2016, **30**, 9596–9604.
22 A. Taguchi and F. Schüth, *Microporous Mesoporous Mater.*, 2005, **77**, 1–45.
23 W. Feng, S. Kwon, E. Borguet and R. Vidic, *Environ. Sci. Technol.*, 2005, **39**, 9744–9748.
24 R. Yan, D. T. Liang, L. Tsen and J. H. Tay, *Environ. Sci. Technol.*, 2002, **36**, 4460–4466.
25 L. Li, T. H. Sun, C. H. Shu and H. B. Zhang, *J. Hazard. Mater.*, 2016, **311**, 142–150.
26 J. Y. Kim, Y. C. Park, S. H. Jo, H. J. Ryu, J. I. Baek and J. H. Moon, *Energy Fuels*, 2016, **30**, 2268–2275.

27 G. J. Mcintosh, G. E. Agbenyegah, M. M. Hyland and J. B. Metson, *Langmuir*, 2015, **31**, 5387–5397.
28 D. Dayananda, V. R. Sarva, S. V. Prasad, J. Arunachalam, P. Parameswaran and N. N. Ghosh, *Appl. Surf. Sci.*, 2015, **329**, 1–10.
29 S. J. Park and S. Y. Jin, *Carbon*, 2004, **42**, 2113–2115.
30 B. Tu, N. Shi, W. Sun, L. Cao and J. Yang, *Environ. Sci. Pollut. Res.*, 2017, **24**, 676–684.
31 W. Dong, X. Chen, F. Yu and Y. Wu, *Energy Fuels*, 2015, **29**, 968–973.
32 A. G. Skerman, S. Heubeck, D. J. Batstone and S. Tait, *Process Saf. Environ. Prot.*, 2017, **105**, 117–126.
33 A. Daneshyar, M. Ghaedi, M. M. Sabzehmeidani and A. Daneshyar, *J. Colloid Interface Sci.*, 2017, **490**, 553–561.
34 M.-T. Lee, Z.-Q. Wang and J.-R. Chang, *Ind. Eng. Chem. Res.*, 2003, **42**, 6166–6170.
35 L. Micoli, G. Bagnasco and M. Turco, *Int. J. Hydrogen Energy*, 2014, **39**, 1783–1787.
36 L. Micoli, G. Bagnasco and M. Turco, *Int. J. Hydrogen Energy*, 2013, **38**, 447–452.
37 C. Zhao, X. Chen and C. Zhao, *Energy Fuels*, 2012, **26**, 1401–1405.
38 C. Zhao, Y. Guo, C. Li and S. Lu, *Appl. Energy*, 2014, **124**, 241–247.
39 C. Zhao, X. Chen and C. Zhao, *Chemosphere*, 2009, **75**, 1401–1404.
40 B. Y. Zhao, D. E. Jiang and Y. C. Xie, *Fuel*, 2002, **81**, 1565–1568.
41 W. Dong, X. Chen, Y. Wu, C. Zhao and C. Liang, *Energy Fuels*, 2012, **26**, 6040–6046.
42 N. Verdone and P. D. Filippis, *Chem. Eng. Sci.*, 2006, **61**, 7487–7496.
43 A. M. Fonseca, J. J. Órfão and R. L. Salcedo, *Ind. Eng. Chem. Res.*, 1998, **37**, 4570–4576.
44 B. L. Dou, J. S. Gao and X. Z. Sha, *Fuel Process. Technol.*, 2001, **72**, 23–33.
45 M. J. D. Low, *Chem. Rev.*, 1980, **60**, 267–312.
46 C. E. Weinell, P. I. Jensen and K. D. Johansen, *Ind. Eng. Chem. Res.*, 1992, **31**, 164–171.